remote sensing

MDPI

Article

Evidence of Widespread Volcanic Activity near Hebrus Valles on Mars Revealed by SHARAD

Stefano Nerozzi [1,*], Michael S. Christoffersen [2], John W. Holt [1] and Christopher W. Hamilton [1]

[1] Lunar and Planetary Laboratory, University of Arizona, Tucson, AZ 85721, USA; jwholt@arizona.edu (J.W.H.); chamilton@arizona.edu (C.W.H.)
[2] Geophysical Institute, University of Alaska Fairbanks, Fairbanks, AK 99775, USA; mchristoffersen@alaska.edu
* Correspondence: nerozzi@arizona.edu

Abstract: Hebrus Valles is an outflow channel system in the plain-forming terrains of southeastern Utopia Planitia, Mars. These terrains may have formed through a combination of liquid water and volcanic processes, yet their nature, subsurface structure, and composition remain unclear. We investigate these terrains by mapping subsurface reflectors across 540 Shallow Radar (SHARAD) profiles and applying two complementary loss tangent inversion techniques. We find moderate loss tangent values across some subregions of Granicus Valles and Hyblaeus Fossae ($\tan\delta = 0.0162 \pm 0.0004$ and $\tan\delta = 0.019 \pm 0.002$, respectively), suggesting the presence of basaltic lava flows. We interpret non-detections in the other flows in Granicus Valles to be due to the presence of radar-lossy materials formed through aqueous processes, which supports the hypothesized occurrence of lahars in this region. A small area near Hebrus Valles exhibits subsurface reflectors with low to moderate loss tangents ($\tan\delta = 0.010 \pm 0.003$), suggesting the presence of pristine lava flows or sedimentary materials capped by lava flows. We also find a widespread occurrence of very low-loss tangent materials near Hyblaeus Dorsa ($\tan\delta = 0.0045 \pm 0.0002$), which may represent a lobe of the Medusae Fossae Formation or similar high-porosity materials buried underneath a lava flow. Together, these findings suggest that volcanic activity played a central role in the formation of terrains across the broader Hebrus Valles region.

Keywords: radar; Mars; loss tangent; lava flows; Hebrus Valles; Granicus Valles; Hyblaeus Fossae; Hyblaeus Dorsa; Medusae Fossae Formation

Citation: Nerozzi, S.; Christoffersen, M.S.; Holt, J.W.; Hamilton, C.W. Evidence of Widespread Volcanic Activity near Hebrus Valles on Mars Revealed by SHARAD. *Remote Sens.* **2023**, *15*, 4967. https://doi.org/10.3390/rs15204967

Academic Editor: Roberto Orosei

Received: 2 September 2023
Revised: 8 October 2023
Accepted: 9 October 2023
Published: 14 October 2023

1. Introduction

Hebrus Valles (HV) is a well-preserved example of an Early Amazonian outflow channel system in southeastern Utopia Planitia (17–25°N, 118–129°E; Figure 1) that is carved into bedrock [1]. The channels exhibit a diverse set of sinuous, anabranching, and rectilinear morphologies indicating that they were formed by one or more liquid water outflow events, possibly due to magmatic intrusions cracking the cryospheric seal of a pressurized aquifer [1–4]. Previous geologic mapping [3,5] indicates that HV carved mainly into two plain-forming units of Late Hesperian to Early Amazonian age, placing a ~3 Ga upper bound on the age of the flows. The channels originate within the oldest of these units, meaning that large amounts of liquid water or water ice must have been present beneath the unit. This older unit also includes lava flows [3,5], indicating that lava–ice interactions may have occurred in the region surrounding HV. Previous studies determined that the youngest unit was emplaced as a fluid flow involving volatiles with widespread occurrences of mud volcanism [3,5,6]. However, radar observations and geologic mapping of terrains north of the channels also indicate the presence of extensive basaltic lava flows and lahars originating from the Elysium mons volcanic edifice [3,7]. Thus, the nature of geologic units surrounding the channels of HV remains unclear, and little is known about their subsurface structure and composition. Additionally, the HV region is located

at low elevation and latitude, comprises extensive and smooth plains, and has moderate dust cover [8], thus meeting first-order criteria for a safe landing target for robotic and human exploration [9,10]. However, the present-day occurrence of shallow water ice, which is key to in situ resource utilization [11], habitability [12], ice stability models [13], and paleoclimate studies [14], is unknown.

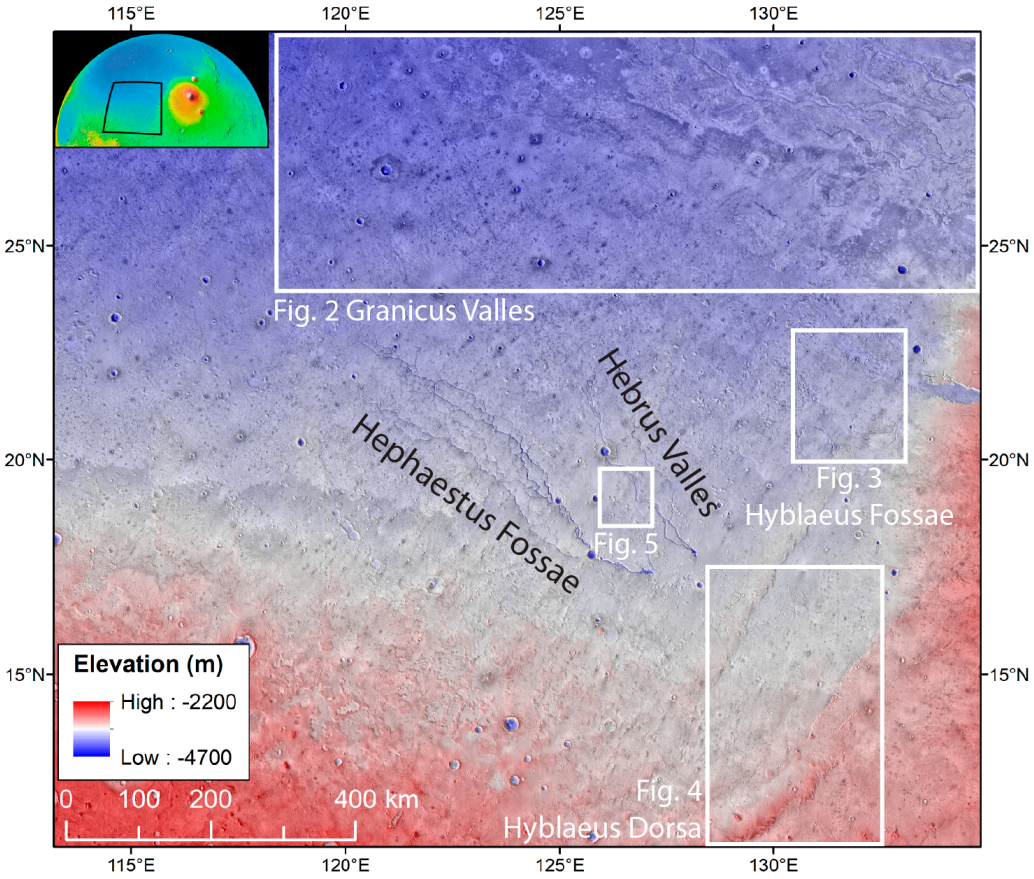

Figure 1. Overview of the study area in THEMIS IR Day mosaic overlain on MOLA–HRSC DTM mosaic in the broader context of Uoptia Planitia. The inset outlines the study location on a perspective view of Mars with warmer colors representing higher elevation. The white boxes show the locations of subsequent figures.

We analyzed 540 Shallow Radar (SHARAD, [15]) profiles over a wide study area surrounding the channels spanning 113°–135°E and 11°–30°N (Figure 1). SHARAD is a sounding radar capable of penetrating the surface to reveal subsurface structures that are otherwise invisible to surface imaging techniques. We also calculated the bulk loss tangent of subsurface materials to constrain their possible composition. SHARAD reveals numerous clusters of subsurface reflectors scattered across the eastern half of the study area, which we divide into three groups based on their location (Figure 1). One large cluster of reflectors is associated with terrains of Granicus Valles and Hyblaeus Fossae, and corresponds to the Elysium Rise unit [3]. At these locations, we measured a wide range of loss tangents that are typical of basaltic lava flows, in agreement with previous geologic mapping interpretations. A second small cluster is located just west of the central section of the HV channels, where we measured a loss tangent also typical of basaltic lava flows. One more cluster of reflectors is located to the SE of HV and reaches much larger depths than all the other radar observations in the study region. We measure a low loss tangent, which suggests the presence of lithic (ice-free), high-porosity, and low-loss materials like those found in the Medusae Fossae Formation (MFF). Overall, radar sounding evidence points to widespread volcanism across the study region.

2. Materials and Methods

2.1. Shallow Radar (SHARAD) Profiles

This work takes advantage of hundreds of 2D profiles over the HV study region that were acquired by SHARAD, onboard the Mars Reconnaissance Orbiter (MRO). SHARAD is an orbital sounding radar with a linear frequency modulation spanning 15–25 MHz, allowing a vertical resolution of ~15 m in free space after pulse compression [15,16]. The horizontal ground resolution after synthetic aperture processing is 0.3–1 km along-track and 3–6 km across-track [15,17]. We use the "U.S. SHARAD" products [18] from the NASA Planetary Data System (PDS), generated by performing aperture focusing and implementing an autofocus ionospheric correction [17]. We choose this SHARAD product due to its advanced ionospheric correction compared to that employed in the alternative Reduced Data Record "Italian" product available in the PDS.

SHARAD detects subsurface interfaces between materials with a contrast in dielectric permittivity that is sufficiently strong to overcome the noise floor of the instrument. Surface topographic relief can also generate reflections that appear at a time delay greater than the nadir surface and may thus be erroneously interpreted as subsurface signals. These signals are commonly referred to as "surface clutter". We employ clutter simulation software that can work with a large variety of digital terrain models (DTMs) [19] and allows us to identify possible sources of clutter and avoid misinterpreting them for subsurface reflectors. Although most of the study region lacks much relief and thus generates only moderate clutter, we follow a conservative approach and use 50 m/pixel DTMs generated from data acquired by the High-Resolution Stereo Camera (HRSC [20]), onboard Mars Express, and 128-pixel/degree Mission Experiment Gridded Data Records (MEGDRs) derived from data acquired by the Mars Orbiter Laser Altimeter (MOLA [21]), onboard the Mars Global Surveyor. Using both datasets ensures that even small clutter sources are simulated, and thus only real subsurface reflectors are mapped.

We import radar profiles into the SeisWare 10.2 suite, a seismic interpretation environment that has proven to be ideal for analyzing and mapping reflectors in SHARAD 2D profiles [22,23]. This software employs a semi-automatic tracing algorithm that helps the interpreter in marking the peak power of a specific reflector with consistency, and can connect profiles at their intersections, thus allowing the tracing of a continuous reflector around areas with strong clutter and/or poor quality of radar returns. To help maintain consistency in reflector tracing, the SeisWare software is set to add subsample smoothing (<37.5 ns) in the vertical axis, sometimes resulting in picks that are in between the nominal 37.5 ns SHARAD sampling interval.

2.2. Loss Tangent Inversions

The loss tangent ($\tan\delta$) is a parameter that describes a material's property to attenuate electromagnetic waves. For typical geologic materials, the loss tangent is mainly influenced by their mineral content (or lack of, in the form of porosity). For example, pure water ice is characterized by very low loss with values < 0.001 [24,25], while basaltic lava flows can have much higher values, ranging from ~0.01 [26,27] to >0.3 [28,29], especially where significant amounts of iron oxides or ilmenite are present [28,30].

We employ two independent and complementary methods to determine the loss tangent of materials sensed by SHARAD, which we italicize throughout the text: *power loss* vs. *time delay* and *subsurface-to-surface power ratio*. We refer to the latter technique as the *power ratio* method in the following sections to be concise. Using two different approaches has multiple benefits. First, each approach represents a trade-off between spatial resolution, uncertainty, and number of assumptions, which combined allow for a robust measurement of the loss tangent. Second, employing two distinct inversion techniques provides redundancy in case one of them performs poorly.

2.2.1. Power Loss vs. Time Delay Method

In the absence of thickness constraints to calculate the full complex dielectric permittivity of a material, it is possible to determine its loss tangent as a function of the observed power loss L, two-way time delay Δt, and center radar wavelength λ [31]:

$$\tan\delta = \sqrt{\left\{2\left[\frac{\lambda}{4\pi c\Delta t}\ln(L)\right]^2 + 1\right\}^2 - 1}. \quad (1)$$

The power loss L can be calculated for each SHARAD profile [31] or a group of reflectors [26] by least-squares-fitting the difference in power between the top and basal surface reflectors as a function of two-way time delay. The error associated with the results of this inversion is estimated as the square root of the diagonal of the least-squares fit of the covariance matrix [32].

2.2.2. Power Ratio Method

The second approach is based on the ratio of estimated power transmitted through the surface and that reflected at the base [33]:

$$\tan\delta = \frac{10\log_{10}(P_t/P_b)}{0.091 f\Delta tc} \quad with \quad P_t = P_s\left[\left(\frac{\sqrt{\varepsilon_s'}+1}{\sqrt{\varepsilon_s'}-1}\right)^2 - 1\right], \quad (2)$$

where P_t is the power transmitted through the surface, P_b is the power measured at the base of the unit, f is the center radar frequency, P_s is the power measured at the surface of the unit, and ε_s' is the real dielectric permittivity of the surface. Typically, ε_s' is estimated based on a plausible composition of the surface. In this study, we use the real dielectric permittivity determined via previous SHARAD surface reflectivity studies [34]. The error associated with the results of this inversion depend on the measurement error of P_b, P_s, and Δt, and the uncertainty of the ε_s' estimate. In this study, we consider the latter uncertainty to be dominant; however, we do not have a reliable estimate of its magnitude. For this reason, we report the 1-σ variability of the inversion results.

2.2.3. Assumptions and Mitigation Strategies

Increased apparent loss may arise due to additional losses from scattering by rough surface and subsurface interfaces. In the study areas, we do not detect the typical diffuse return caused by surface scattering. Additionally, the power loss vs. time delay method described in Section 2.2.1 is independent of surface or subsurface interface roughness because it depends only on the rate of loss vs. time delay. Additional losses may arise from volume scattering but, again, we do not detect any evidence of this phenomenon occurring within the study area in the form of diffuse scattering. The power ratio method is instead susceptible to surface scattering losses, but it has been demonstrated that these contributions become negligible at increasing thicknesses [35], and thus the real subsurface loss tangent can be determined by plotting it against the two-way time delay and measuring it where it becomes asymptotic.

Additionally, loss tangent inversions are often performed assuming the central frequency of the radar. However, SHARAD operates across a wide range of frequencies and the power spectrum is known to be non-uniform with as much as 3 dB of variability [27]. We take this aspect into account by iterating the loss tangent inversion methods across the entire SHARAD chirp spectrum and performing a weighted average that depends on the calibrated chirp power spectrum available in the PDS, as performed in recent studies [36].

2.2.4. Mapping and Subdivision of Reflector Clusters and Further Clutter Rejection

We employ Mars Odyssey's Thermal Emission Imaging System (THEMIS, [37]) infrared dayside global mosaic [38] to guide the SHARAD subsurface reflector mapping. This

dataset allows us to classify and subdivide terrains and reflectors within them based on their thermophysical properties, which is the combination of thermal inertia and physical morphology. First, we treat reflectors found within a terrain with consistent thermophysical properties as a single group representing radar echoes arising from the same dielectric interface. Then, we verify that reflectors are laterally continuous and have consistent shapes and depths within intersecting radargrams, which helps to identify clutter that was not predicted by simulations, because clutter two-way time delay tends to shift much more than subsurface reflectors in adjacent profiles.

3. Results

We identify subsurface reflectors across four main regions within the study area, each containing one or more clusters of subsurface reflectors: Granicus Valles and Hyblaeus Fossae, Hebrus Valles, and Hyblaeus Dorsa. We present the results of loss tangent inversions subdivided by region below and in Table 1. Instead of calculating the loss tangent for each radar profile (as done in [31]), we prefer to use all subsurface reflectors in each cluster, which yields more robust results thanks to the larger number of samples [26].

Table 1. Summary of loss rates and loss tangents calculated in each study region and subregion.

Region		Loss Rate (dB/µs)	Loss Tangent *Power Loss* vs. *TWT*	Loss Tangent *Power Ratio*	Loss Tangent *Power Ratio at Max TWT* [1]
Granicus Valles	A	15.2 ± 2.2	0.028 ± 0.004	0.027 ± 0.006	~0.017
	B	9.4 ± 4.0	0.017 ± 0.007	0.015 ± 0.002	n/a
	C	8.1 ± 1.8	0.015 ± 0.003	0.016 ± 0.004	~0.010
	D	7.9 ± 1.1	0.015 ± 0.002	0.015 ± 0.004	n/a
	E	11.3 ± 2.1	0.021 ± 0.004	0.016 ± 0.004	n/a
	F	7.0 ± 2.4	0.013 ± 0.004	0.010 ± 0.002	n/a
	G	11.5 ± 0.6	0.021 ± 0.001	0.020 ± 0.005	~0.010
	H	8.2 ± 1.5	0.015 ± 0.003	0.021 ± 0.004	n/a
	I	6.2 ± 0.9	0.011 ± 0.002	0.012 ± 0.003	n/a
	J	7.7 ± 1.1	0.014 ± 0.002	0.022 ± 0.006	~0.013
	K	15.0 ± 2.1	0.027 ± 0.004	0.017 ± 0.004	n/a
	L	7.3 ± 0.7	0.013 ± 0.001	0.017 ± 0.006	~0.009
	M	7.4 ± 1.5	0.014 ± 0.003	0.021 ± 0.006	~0.013
	N	5.6 ± 1.0	0.010 ± 0.002	0.015 ± 0.004	~0.008
	O	13.7 ± 0.9	0.025 ± 0.002	0.020 ± 0.007	~0.010
	All [2]	*8.9 ± 0.2*	*0.0162 ± 0.0004*	*0.018 ± 0.006*	*~0.008*
Hyblaeus Fossae		10.6 ± 0.8	0.019 ± 0.002	0.020 ± 0.007	n/a
Hebrus Valles		5.5 ± 1.5	0.010 ± 0.003	0.014 ± 0.005	~0.010
Hyblaeus Dorsa		2.5 ± 0.1	0.0045 ± 0.0002	0.007 ± 0.004	~0.005

[1] These loss tangent values are an estimate based on the asymptotic shape of the loss tangent vs. TWT curve obtained using the *power ratio* method. Therefore, these values are affected by subjective interpretation errors. [2] These results include all sub-regions in Granicus Valles, and thus may represent an average of significantly different materials.

3.1. Granicus Valles and Hyblaeus Fossae

Granicus Valles is in the northernmost reaches of the study area, ~200 km north of the distal section of the HV channels. Here, we found numerous subsurface reflectors across a variety of landforms that are collectively associated with Elysium rise volcanic flow units in previous geologic maps [3,39] and are distributed in small clusters that appear to correspond with smooth and high-thermal-inertia terrains (Figure 2a–c). For this reason, we subdivided the reflectors into subregions based on thermophysical properties of terrains seen in the THEMIS IR day v12 and night v14 mosaics [38], allowing us to examine the radar characteristics of each cluster.

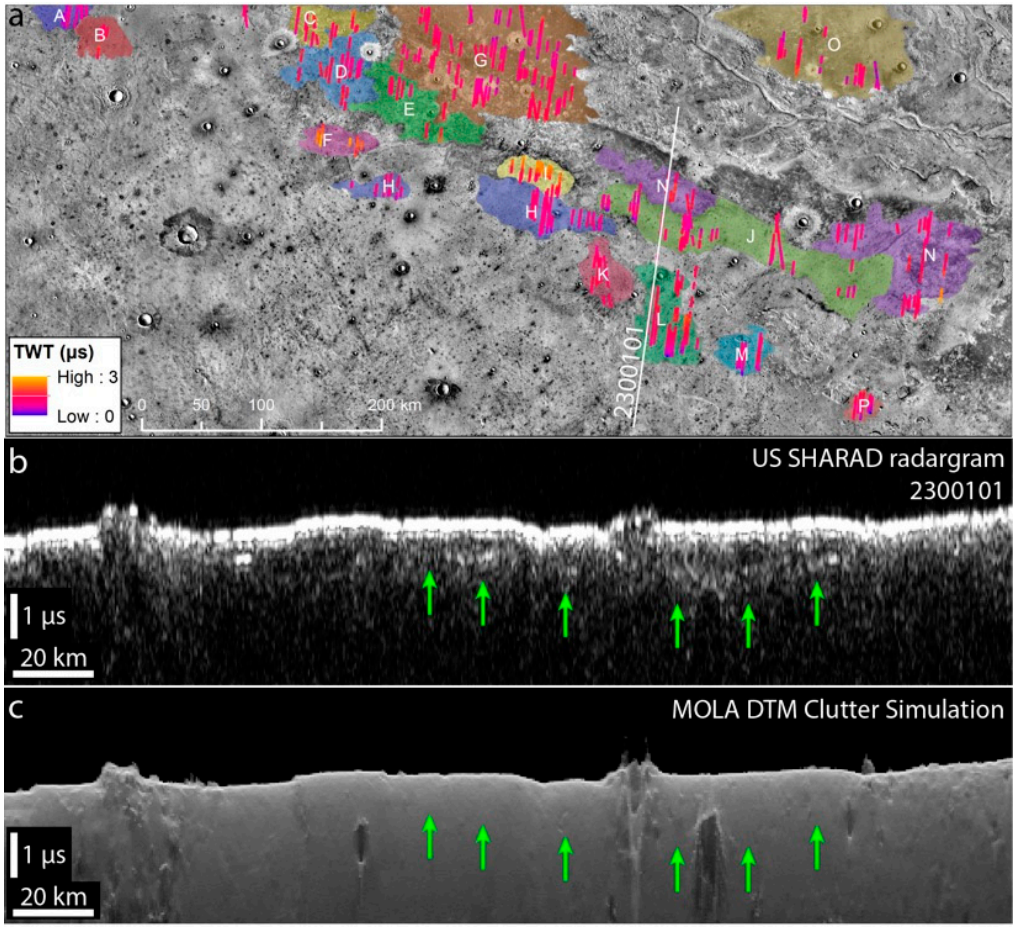

Figure 2. Shallow Radar (SHARAD) subsurface reflector mapping and loss tangent analysis in Granicus Valles. (**a**) Thermal Emission Imaging System (THEMIS) infrared (IR) daytime view of Granicus Valles with mapped clusters of reflectors (shown with colors corresponding to two-way-time, TWT) and the location of the profile shown in panels (**b**,**c**). Each cluster is associated with a letter from A to P and loss tangent results can be found in Table 1. (**b**) Sample of SHARAD profile 2300101 with multiple discontinuous subsurface reflectors and (**c**) corresponding Mars Orbiter Laser Altimeter (MOLA) clutter simulation.

The mean loss tangent measured in Granicus Valles with the *power loss* vs. *time delay* method is 0.0162 ± 0.004 (Figure 3a), and ranges from a minimum of ~0.010 for subregion N to a maximum of ~0.027 for subregions K and A (Figure 3b). The *power ratio* method yields a similar mean loss tangent of 0.0183 ± 0.0059 when assuming a surface ε'_s = 3.5 (Figure 3c), which we selected based on the ε'_s = 3–4 range measured by prior studies in this region [34,40]. However, the loss tangent decreases to a value of ~0.01 at larger two-way time delays (Figure 3d).

We detect only one small cluster of reflectors in Hyblaeus Fossae, which lies on the same Elysium rise volcanic flow units as the Granicus Valles region [3,39]. Unlike most clusters in Granicus Valles, the reflectors in this region occur within a relatively low thermal inertia terrain (Figure 4a).

We obtain a mean loss tangent in Hyblaeus Fossae of 0.0194 ± 0.0015 based on the *power loss* vs. *time delay* method (Figure 4b), and 0.0204 ± 0.0071 using the *power ratio* method and assuming a surface ε'_s = 3.5 (Figure 4c).

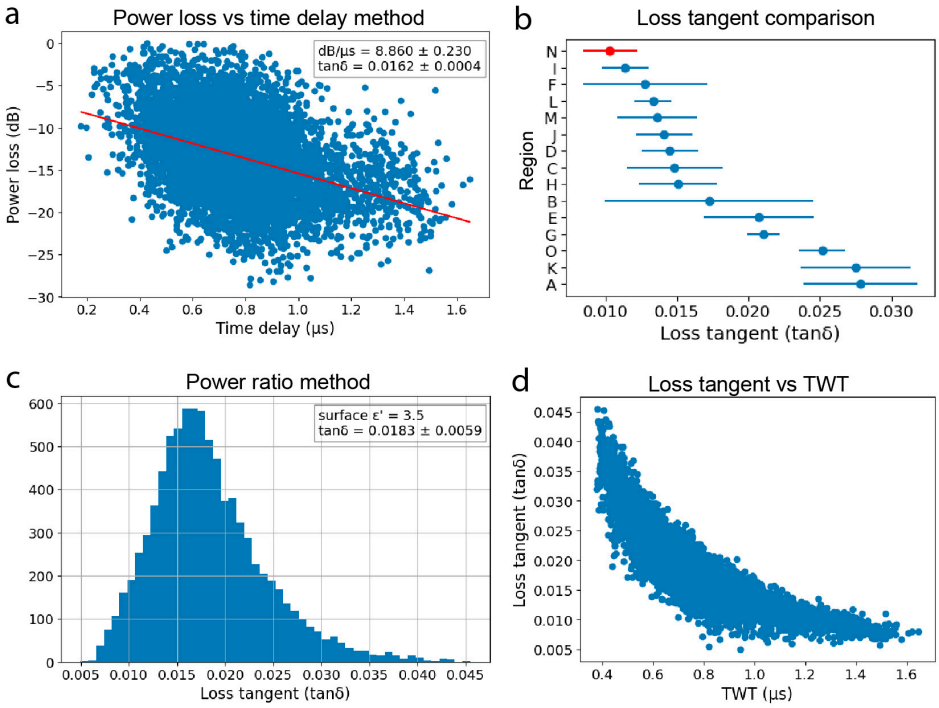

Figure 3. Loss tangent inversions in Granicus Valles. (**a**) Plot of measured surface to subsurface power loss vs. time delay for all reflectors in Granicus Valles and resulting loss tangent calculated with the *power loss vs. time delay* method. (**b**) Comparison of loss tangents calculated across each region shown in Figure 2a. (**c**) Histogram of bulk loss tangent for the entire Granicus Valles region using the *power ratio* method and plot of the same results vs. two-way travel time. (**d**) Plot of loss tangent, calculated with the *power loss vs. time delay* method, vs. two-way time (TWT) delay.

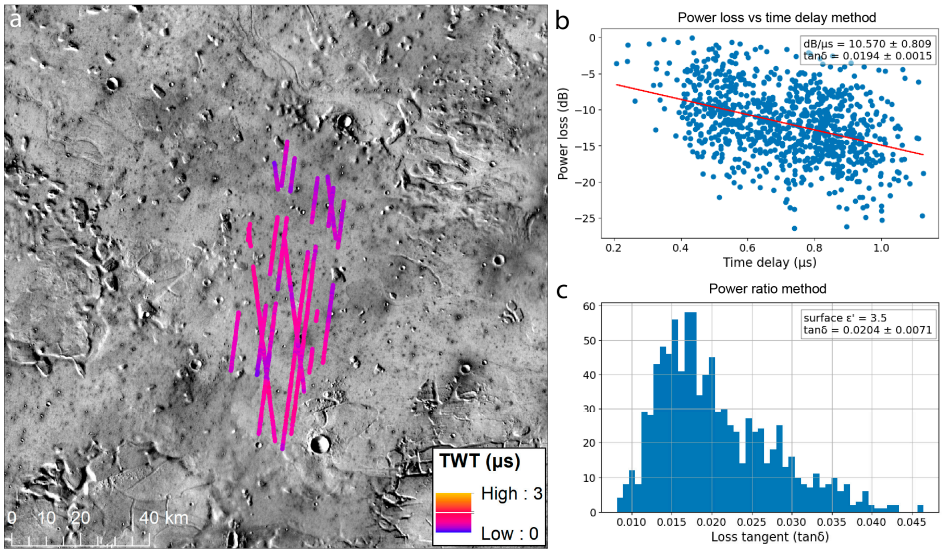

Figure 4. SHARAD subsurface reflector mapping and loss tangent analysis in Hyblaeus Fossae. (**a**) THEMIS IR Day view of Hyblaeus Fossae with mapped reflectors. Note that the reflectors occur within a terrain with lower thermal inertia than its surrounding. (**b**) Plot of measured surface to subsurface power loss vs. time delay for all reflectors in Hyblaeus Fossae and resulting loss tangent calculated with the *power loss vs. time delay* method. (**c**) Histogram of bulk loss tangent calculated using the power ratio method.

3.2. Hebrus Valles

We find a small cluster of reflectors just W of the central section of Hebrus Valles channels (Figure 5a). These reflectors are characterized by a low signal-to-noise ratio (SNR) compared to background noise and clutter (Figure 5b), but it was still possible to trace them thanks to the high-resolution clutter simulation based on MOLA and HRSC DTMs (Figure 4c,d). Like the Hyblaeus Dorsa region, these reflectors occur underneath smooth plain-forming terrains and appear to deepen slightly in the NW direction (Figure 4a,b). THEMIS thermal infrared imagery does not show any systematic change in thermal inertia across this area aside from a discontinuous dusty ejecta ray originating from the Tomini impact. The spatial distribution of subsurface reflectors does not appear to be related to this ejecta ray.

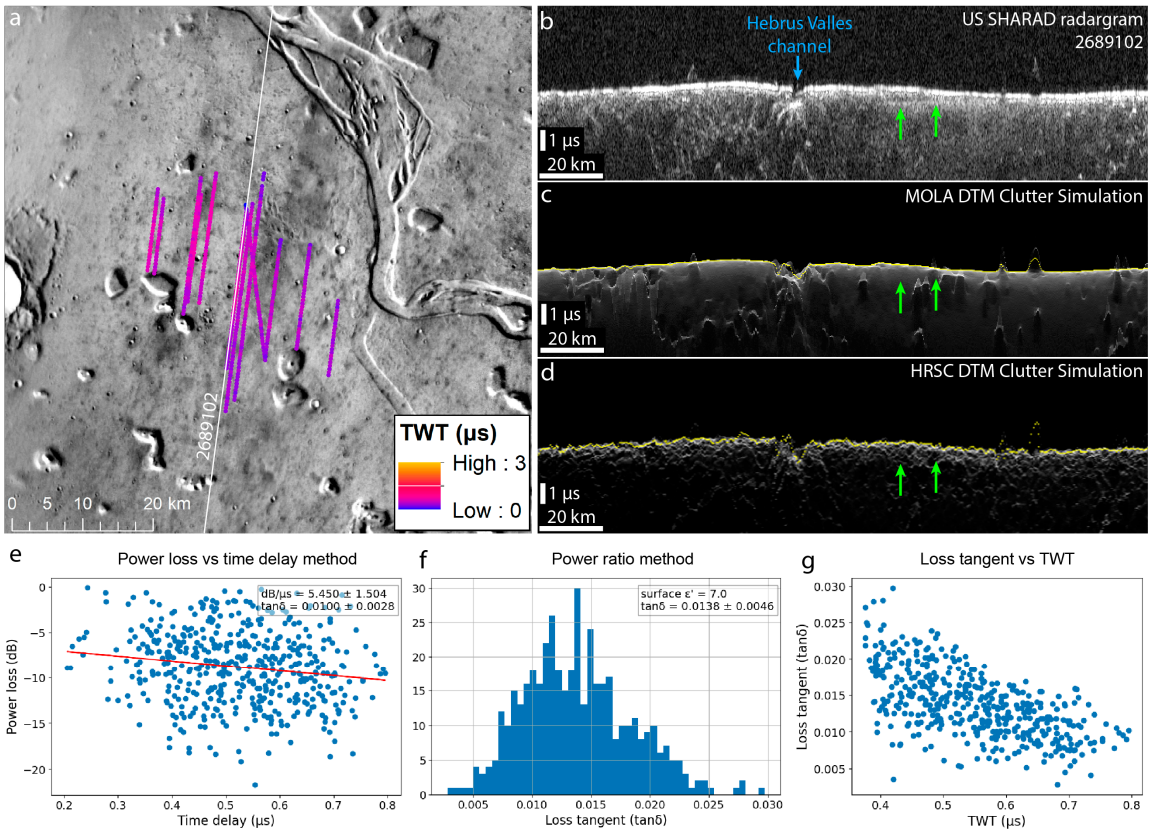

Figure 5. SHARAD subsurface reflector mapping and loss tangent analysis near Hebrus Valles. (**a**) THEMIS IR Day view of Hebrus Valles and surrounding terrains with mapped reflectors. (**b**) Sample of SHARAD profile 2689102 showing a nearly flat reflector (location in panel (**a**)) and corresponding (**c**) MOLA and (**d**) HRSC clutter simulation. (**e**) Plot of measured surface to subsurface power loss vs. time delay for all reflectors near Hebrus Valles and resulting loss tangent calculated using the *power loss vs. time delay* method. (**f**) Histogram of bulk loss tangent calculated using the *power ratio* method, and (**g**) plot of the same results vs. two-way time delay.

The mean loss tangent measured for this reflector cluster using the *power loss* vs. *time delay* method is 0.0100 ± 0.0028 (Figure 5e). The *power ratio* method yields a higher mean loss tangent of 0.0138 ± 0.0046 when assuming a surface $\varepsilon'_s = 7$ (Figure 5f), which is the average value of the $\varepsilon'_s = 6$–8 range measured by previous studies in this region [34], but decreasing to ≤0.01 at the largest two-way time delay of ~0.8 µs (Figure 5g).

3.3. Hyblaeus Dorsa

The last cluster of reflectors found in this study is located near Hyblaeus Dorsa, a prominent wrinkle ridge extending in the NE–SW direction across the northern plains

of southeastern Utopia Planitia (Figure 1). Subsurface reflectors are detected across the smoothest areas of plain-forming terrains just NW of Hyblaeus Dorsa and deepen toward the NE (Figure 6a–c). We find chaos terrain in the same area, but there are no reflectors underneath them. We do not detect any significant change in thermal inertia across this area.

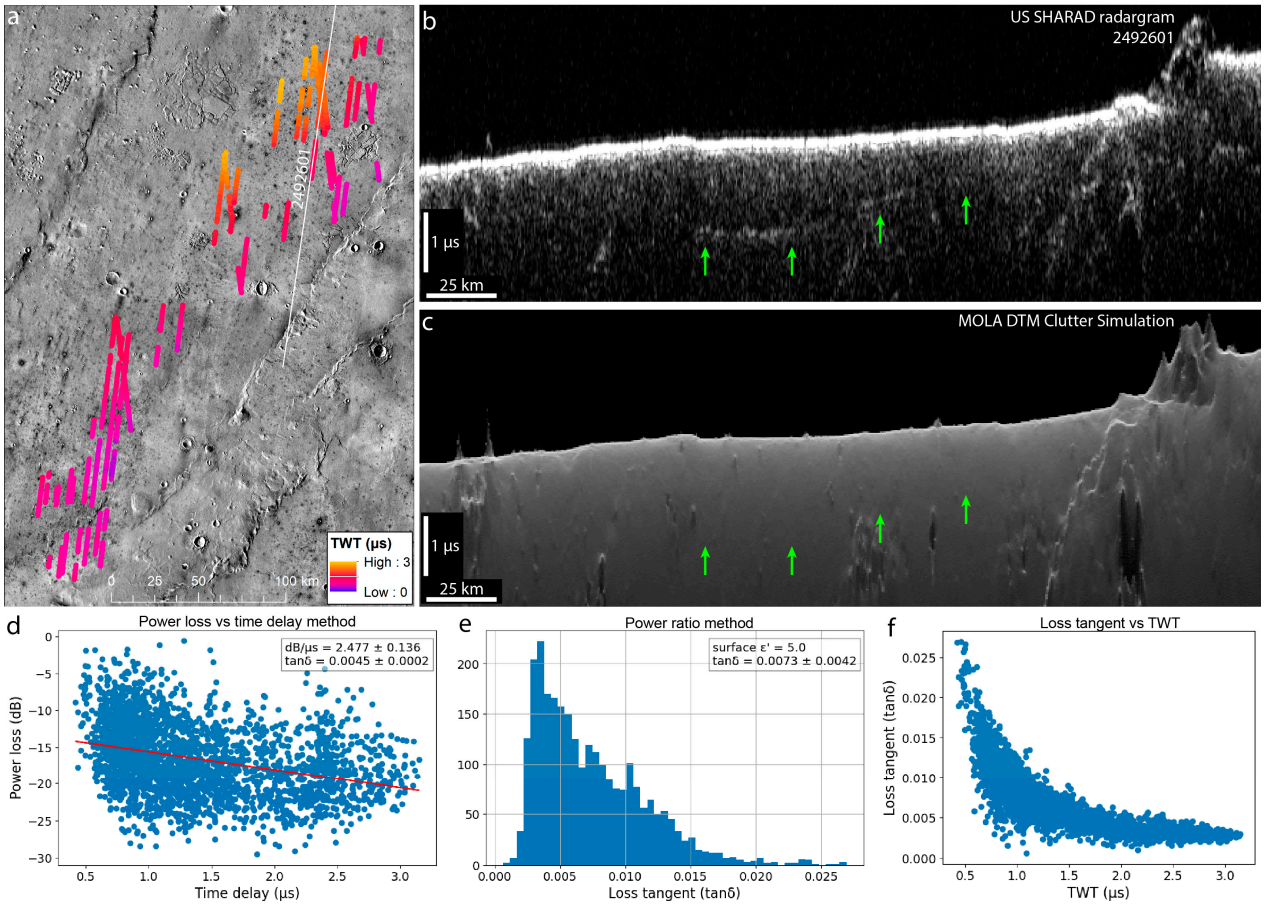

Figure 6. SHARAD subsurface reflector mapping and loss tangent analysis near Hyblaeus Dorsa. (**a**) THEMIS IR Day view of Hyblaeus Dorsa with mapped reflectors. (**b**) Sample of SHARAD profile 2492601 showing a single dipping reflector (location in panel a) and (**c**) corresponding MOLA clutter simulation. (**d**) Plot of measured surface to subsurface power loss vs. time delay for all reflectors in Hyblaeus Dorsa and resulting loss tangent calculated using the *power loss vs. time delay* method. (**e**) Histogram of bulk loss tangent for the entire Granicus Valles region calculated using the *power ratio* method, and (**f**) plot of the same results vs. two-way time delay.

In this region, we measure a mean loss tangent of 0.0045 ± 0.0002 via the *power loss* vs. *time delay* method (Figure 6d) and 0.0073 ± 0.0042 via the *power ratio* method (Figure 6e) with a surface $\varepsilon'_s = 5$ previously measured in this region [34] but decreasing asymptotically to ~0.005 at larger two-way time delays (Figure 6f).

4. Discussion

4.1. Granicus Valles and Hyblaeus Fossae

Thermophysical mapping of the Granicus Valles region based on THEMIS IR images indicate that these materials belong to several distinct flows, each with characteristic morphologies and thermal inertia. There is also a wide range of loss tangents calculated using the *power loss* vs. *time delay* method, spanning from ~0.01 to ~0.03. There is a partial inconsistency between the loss tangent values obtained via the two inversion techniques, although both indicate that the loss tangent is larger than ~0.01 everywhere. In general,

the entire range of loss tangent values measured in this region is compatible with a variety of basaltic lava flows found elsewhere on Mars [26,27,41], and is in agreement with the findings of prior SHARAD subsurface analyses of the northwestern reaches of Granicus Valles [40] and geologic mapping of the entire region, suggesting a volcanic origin of these terrains [3,42]. Explaining the wide range of loss tangents and the partial inconsistency of results requires a closer examination of the thermophysical properties of this region and its geologic context. Reflectors in Granicus Valles occur underneath some flows but not others, meaning that characteristics of the surface (e.g., roughness, mantling) and/or the subsurface (e.g., high loss mineral content, lack of dielectric contrasts) vary across this region.

A previous study of Martian mid-latitude glacial debris covers showed that surface roughness at scales similar to SHARAD wavelengths can cause large losses even if no significant scattering is observed along profiles [43]. Similarly, mantling by lithic fines was found to be effective at reducing surface losses in Tharsis [26]; however, the wide range of thermal inertia found across each sub-region in Granicus Valles suggests that these are not dominant mechanisms. In the subsurface, large dielectric permittivity contrasts may arise from weathering and/or mantling by fine materials or regolith between lava flows, as found previously in Elysium Planitia [44] and Tharsis [26], or at the contact between materials with drastically different porosity (e.g., vesiculated vs. dense lava flows, [41]). We find it unlikely that these dielectric interfaces are missing from all the Granicus Valles flows lacking subsurface reflectors.

Losses could also arise from the presence of radar-absorbing materials such as clays and hydrated minerals [45], which may occur at the surface in the form of coatings or weathering layers, or in the subsurface. Indeed, previous geologic mapping found that Granicus Valles formed by lahars in combination with lava flows [3,42], suggesting that lossy materials derived from aqueous alteration within lahars may be responsible for the lack of SHARAD's signal along some flows. Thus, we hypothesize that SHARAD detects subsurface interfaces in Granicus Valles only along relatively pristine lava flows (i.e., no aqueous alternation), while the "reflector-free" areas represent weathered lava flows or lahar deposits. The materials examined in Hyblaeus Fossae are also known to be part of the Elysium rise lava flows [3], although, in this case, the low thermal inertia compared to surrounding terrains suggests the presence of a lithic fine mantling (e.g., dust), which smoothens surface roughness and enhances radar subsurface penetration as observed in Tharsis [26].

4.2. Hebrus Valles

SHARAD detects subsurface interfaces only in one small area near the outflow channels of Hebrus Valles and Hephaestus Fossae. These terrains do not bear any distinct textures, morphologies, or thermal properties that distinguish them from their surroundings. This area lies ~100 km uphill from the nearest distributary channels of Hebrus Valles and there is no evidence of fluvial deposition, for example, originating from an avulsion, nor erosion. The reflectors do not reach the channels (Figure 2a,b) and the channel erosional walls do not expose any remarkable or distinct subsurface stratigraphy. The absence of surface clues, the small extent of this area, and the fact that this is the only occurrence of SHARAD reflectors near the channels indicate that the subsurface has unique characteristics.

One possible explanation is that these terrains bear water ice, perhaps a remnant from the water flows that carved Hebrus Valles. However, if this was the case, we would expect to detect more water ice deposits near the channels and especially in their distributary region. Additionally, subsurface water ice stability models show that water ice is not stable at <280 m depths at these latitudes [46], well beyond the ~70 m maximum depth of reflectors assuming a bulk pure water ice composition ($\varepsilon' = 3.0$; [47]). This is confirmed at shallow depths by the lack of exposed ice from recent impacts at low latitudes [48,49]. Thus, we exclude that the reflectors originate from the contact between an ice-rich unit and

bedrock below it, or the top of an ice table (the reflectors pinch out toward the surface at some locations, Figure 5b).

The moderate loss tangent values of ~0.01 measured at this location suggest the presence of basaltic materials analogous to the low-loss lava flows found near Acraeus Mons [26] and in Elysium Planitia [27] or sedimentary materials capped by lava flows found in Amazonis Planitia [27,31] (Figure 7). The results obtained via the *power ratio* method indicate that the effective loss tangent at depth—where the losses at the surface become less important—is likely lower than 0.01. This value is very similar to the lava-capped sediments of Amazonis Planitia [31] and, thus, we favor this scenario. Due to the lack of distinct thermophysical properties of this area, the high thermal inertia signature of the capping lava flow must be masked by a dust or regolith layer. It remains unclear why reflectors appear only in this area, but we can speculate that lava flows could have protected the underlying sediments from extensive weathering and thus inhibited the formation of high-loss minerals that limit the penetration of SHARAD radio waves elsewhere in the study area.

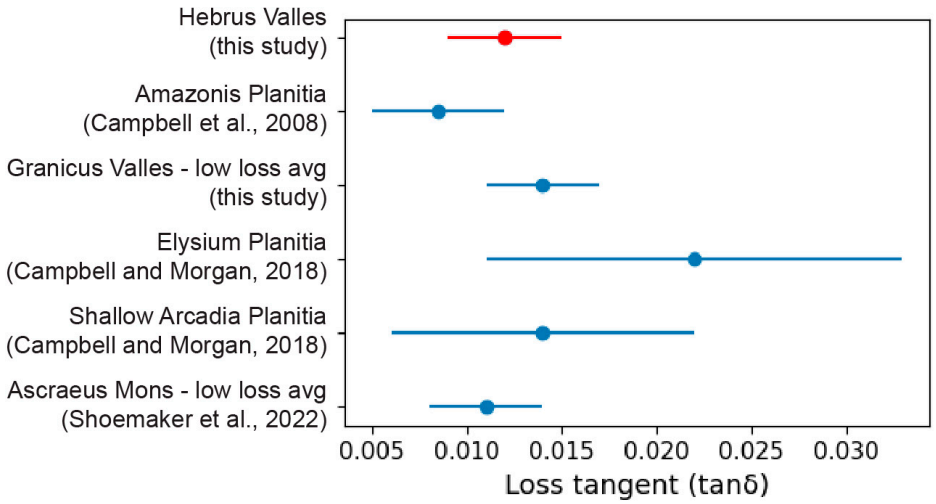

Figure 7. Comparison of loss tangents obtained in this study in the Hebrus Valles region with those by previous studies of a variety of Martian volcanic provices and planitiae [26,27,31].

4.3. Hyblaeus Dorsa

The loss tangent measured in Hyblaeus Dorsa is significantly lower than those in every other region examined in this study. These results can be explained by the presence of either water ice with small impurity content or high-porosity dry lithic materials with low-loss mineral content. Like the Hebrus Valles case, we exclude the presence of significant water ice content in this region due its long-term instability at very low latitudes (12°–17° N) [46]. Additionally, unlike Hebrus Valles, we do not find any evidence of the presence of water in liquid or solid form in this region. Instead, we find that the low loss tangent values of ~0.005 are fully compatible with the values measured for the Medusae Fossae Formation (MFF) in North Hill and Amazonis Mensa [27] and Eumenides Dorsum [50], or materials in the deepest reaches of Arcadia Planitia [27] (Figure 8).

The MFF straddles the Martian topographic dichotomy and extends longitudinally from 140°E to 230°E, with Aeolis Planum being the closet occurrence ~800 km SE of Hyblaeus Dorsa (Figure 9). We find it plausible that MFF or MFF-like materials infill a basin near Hyblaeus Dorsa and are capped by lava flows or other mechanically resistant materials that are not as prone to erosion as the MFF. The capping could be responsible for higher loss tangents, especially those found at low depth via the *power ratio* method (Figure 6f), compared to most MFF materials [50]. Modeled volcanic ash dispersal patterns originating from Apollinaris Pathera show that these low-density materials may have accumulated as far west as Hyblaeus Dorsa [51]. Similarly, eruptions from the Elysium volcanic complex

may have released ash in this region, suggesting once again that volcanic processes are likely responsible for the formation of terrains across the broader Hebrus Valles study area.

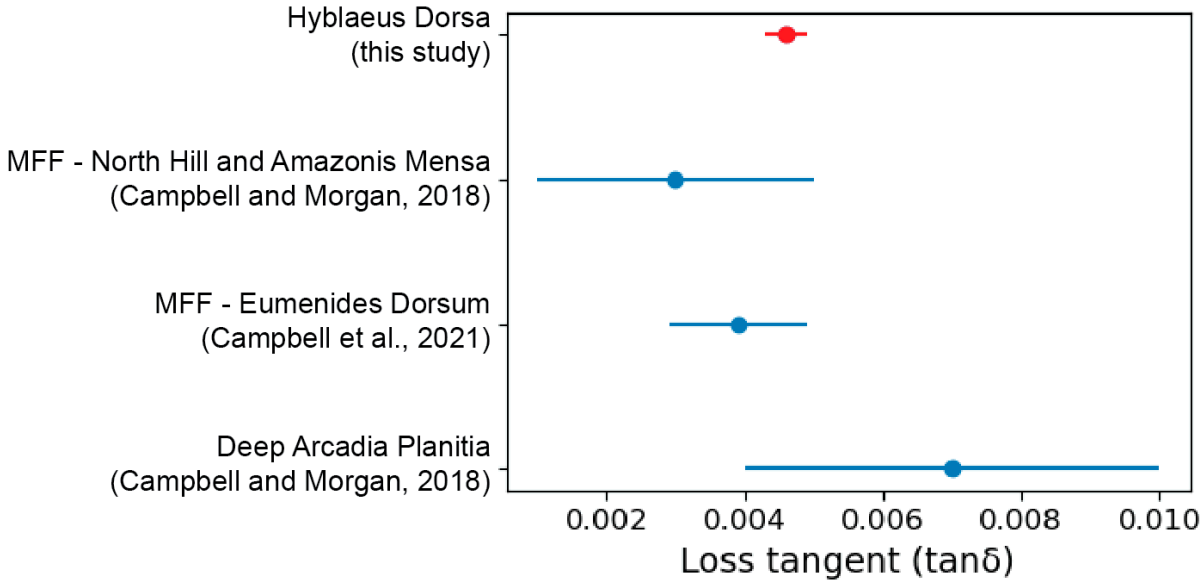

Figure 8. Comparison of loss tangents obtained in this study in the Hyblaeus Dorsa region with those by previous studies of the Medusae Fossae Formation and Arcadia Planitia [27,50].

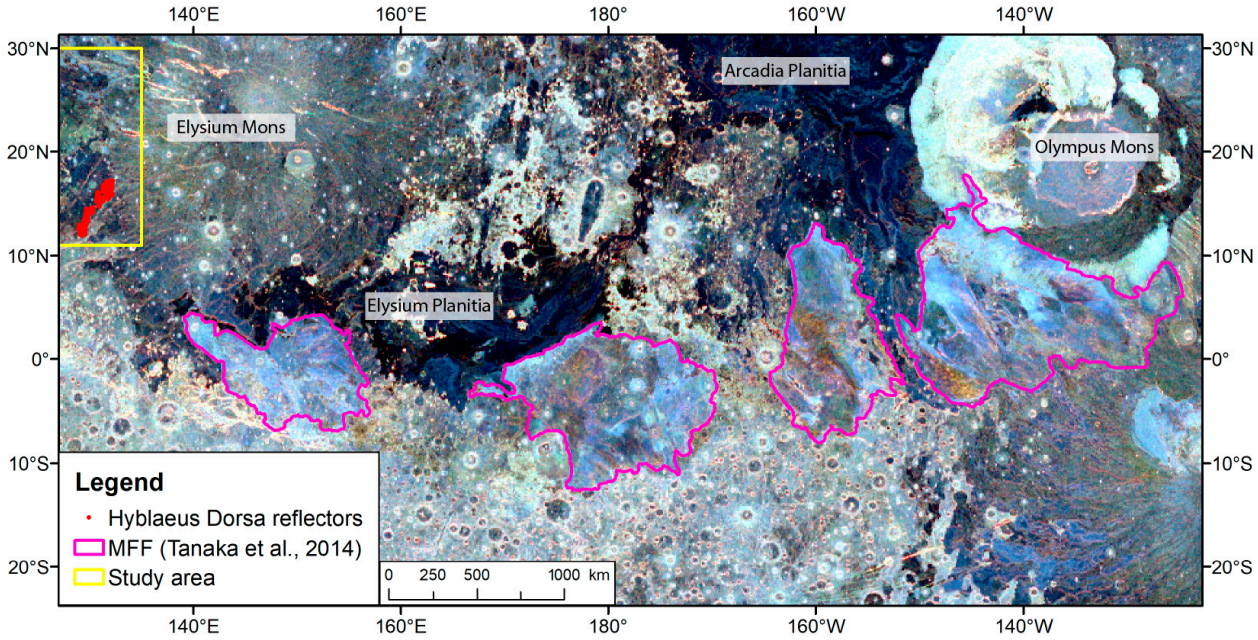

Figure 9. Map of MOLA roughness (represented with RGB colors) calculated at 0.6 km (blue), 2.4 km (green), and 9.6 km (red) [52] with mapped extent of the Medusae Fossae Formation [39] and SHARAD reflectors found in Hyblaeus Dorsa. Note that the reflectors mapped in this study are located near the Martian topographic dichotomy, similar to the Medusae Fossae Formation. The study area (yellow box) extends beyond the western edge of the map.

5. Conclusions

SHARAD detects evidence of basaltic materials with a wide variety of loss tangents across large swaths of the broader Hebrus Valles region. We find evidence of widespread materials with moderate loss tangents that are best explained with the presence of relatively pristine lava flows in Granicus Valles and Hyblaeus Fossae. Lava flows may also cap and

protect sedimentary materials from alteration near Hebrus Valles. Additionally, we find the widespread occurrence of very low-loss tangent materials near Hyblaeus Dorsa, which may represent a lobe of Medusae Fossae Formation or similar high-porosity materials buried underneath a lava flow. These results indicate that volcanic activity played a central role in the formation of terrains across this region.

Supplementary Materials: The following supporting information can be downloaded at https://www.mdpi.com/article/10.3390/rs15204967/s1. Supplementary information including a note on the SHARAD chirp power spectrum and loss tangent results for each Granicus Valles sub-region can be found in supplementary_information.pdf. Original data produced by this study can be found in supplementary_data.zip. The Python 3 code used to calculate loss tangents and generate plots can be found in the following Zenodo-GitHub repository: https://doi.org/10.5281/zenodo.8310445.

Author Contributions: Conceptualization, methodology, formal analysis, writing—original draft preparation, project administration, S.N.; software, writing—review and editing, M.S.C.; writing—review and editing, J.W.H. and C.W.H.; funding acquisition, S.N., J.W.H. and C.W.H. All authors have read and agreed to the published version of the manuscript.

Funding: This research was funded by the NASA Mars Data Analysis Program, grant number 80NSSC19K1220.

Data Availability Statement: The data used in this work are available publicly through the PDS (https://pds.nasa.gov/). Processed data are attached as supplementary material.

Acknowledgments: We are grateful to SeisWare, Inc., for providing the licensing to the interpretation software used for the SHARAD profile analysis. SHARAD was provided to NASA's Mars Reconnaissance Orbiter mission by the Italian Space Agency (ASI). We thank two anonymous reviewers whose constructive comments improved the explanation of the methodology and results.

Conflicts of Interest: The authors declare no conflict of interest.

References

1. Christiansen, E.H.H. The Origin of Channels and Associated Deposits in the Elysium Region of Mars; NASA Final Technical Report. 1987. Available online: https://ntrs.nasa.gov/citations/19870019962 (accessed on 1 October 2023).
2. Carr, M.H.; Malin, M.C. Meter-Scale Characteristics of Martian Channels and Valleys. *Icarus* **2000**, *146*, 366–386. [CrossRef]
3. Tanaka, K.L.; Skinner, J.A.; Hare, T.M. *Geologic Map of the Northern Plains of Mars*; Information Services distributor; US Geological Survey: Reston, VA, USA, 2005.
4. Rodriguez, J.A.P.; Bourke, M.; Tanaka, K.L.; Miyamoto, H.; Kargel, J.; Baker, V.; Fairén, A.G.; Davies, R.J.; Bridget, L.; Santiago, R.L.; et al. Infiltration of Martian outflow channel floodwaters into lowland cavernous systems. *Geophys. Res. Lett.* **2012**, *39*, L22201. [CrossRef]
5. Skinner, J.A.; Tanaka, K.L. *Geologic Map of the Nepenthes Planum Region, Mars*; Scientific Investigations Map; US Geological Survey: Reston, VA, USA, 2018.
6. Kreslavsky, M.A.; Head, J.W. Fate of outflow channel effluents in the northern lowlands of Mars: The Vastitas Borealis Formation as a sublimation residue from frozen ponded bodies of water. *J. Geophys. Res. Planets* **2002**, *107*, 5121. [CrossRef]
7. Nunes, D.C.; Smrekar, S.E.; Safaeinili, A.; Holt, J.; Phillips, R.J.; Seu, R.; Campbell, B. Examination of gully sites on Mars with the shallow radar. *J. Geophys. Res. Planets* **2010**, *115*, E10004 1-20. [CrossRef]
8. Ruff, S.W.; Christensen, P.R. Bright and dark regions on Mars: Particle size and mineralogical characteristics based on Thermal Emission Spectrometer data. *J. Geophys. Res. Planets* **2002**, *107*, 2-1–2-22. [CrossRef]
9. Cockell, C.; Bridges, J.; Dannatt, L.; Burchell, M.; Patel, M.; Danson, M. Where to land on Mars. *Astron. Geophys.* **2009**, *50*, 6.18–6.26. [CrossRef]
10. Davila, A.; Fairén, A.G.; Rodríguez, A.P.; Schulze-Makuch, D.; Rask, J.; Zavaleta, J. The Hebrus Valles Exploration Zone: Access to the Martian Surface and Subsurface. In Proceedings of the First Landing Site/Exploration Zone Workshop for Human Missions to the Surface of Mars, Houston, TX, USA, 27–30 October 2015; Volume 1879, p. 1012.
11. Zubrin, R. Local Resource Creation on Mars. In *Handbook of Space Resources*; Badescu, V., Zacny, K., Bar-Cohen, Y., Eds.; Springer International Publishing: Cham, Switzerland, 2023; pp. 669–687. ISBN 978-3-030-97913-3.
12. Westall, F.; Loizeau, D.; Foucher, F.; Bost, N.; Betrand, M.; Vago, J.; Kminek, G. Habitability on Mars from a Microbial Point of View. *Astrobiology* **2013**, *13*, 887–897. [CrossRef]
13. Schorghofer, N.; Forget, F. History and anatomy of subsurface ice on Mars. *Icarus* **2012**, *220*, 1112–1120. [CrossRef]
14. Becerra, P.; Smith, I.B.; Hibbard, S.; Andres, C.; Bapst, J.; Bramson, A.M.; Buhler, P.B.; Coronato, A.; Diniega, S.; Emmett, J.; et al. Past, Present, and Future of Mars Polar Science: Outcomes and Outlook from the 7th International Conference on Mars Polar Science and Exploration. *Planet. Sci. J.* **2021**, *2*, 209. [CrossRef]

15. Seu, R.; Phillips, R.J.; Biccari, D.; Orosei, R.; Masdea, A.; Picardi, G.; Safaeinili, A.; Campbell, B.A.; Plaut, J.J.; Marinangeli, L.; et al. SHARAD sounding radar on the Mars Reconnaissance Orbiter. *J. Geophys. Res. Planets* **2007**, *112*, E05S05. [CrossRef]
16. Seu, R.; Biccari, D.; Orosei, R.; Lorenzoni, L.V.; Phillips, R.J.; Marinangeli, L.; Picardi, G.; Masdea, A.; Zampolini, E. SHARAD: The MRO 2005 shallow radar. *Planet. Space Sci.* **2004**, *52*, 157–166. [CrossRef]
17. Campbell, B.A.; Putzig, N.E.; Carter, L.M.; Phillips, R.J. Autofocus Correction of Phase Distortion Effects on SHARAD Echoes. *IEEE Geosci. Remote Sens. Lett.* **2011**, *8*, 939–942. [CrossRef]
18. Campbell, B.U.S. *Shallow Radar (SHARAD) Data Product Description for the Planetary Data System*; Smithsonian Institute: Washington, DC, USA, 2014.
19. Choudhary, P.; Holt, J.W.; Kempf, S.D. Surface Clutter and Echo Location Analysis for the Interpretation of SHARAD Data From Mars. *IEEE Geosci. Remote Sens. Lett.* **2016**, *13*, 1285–1289. [CrossRef]
20. Neukum, G.; Jaumann, R. HRSC: The High Resolution Stereo Camera of Mars Express. In *Mars Express: The Scientific Payload*; ESA Publications Division: Noordwijk, The Netherlands, 2004; Volume 1240, pp. 17–35.
21. Smith, D.E.; Zuber, M.T.; Frey, H.V.; Garvin, J.B.; Head, J.W.; Muhleman, D.O.; Pettengill, G.H.; Phillips, R.J.; Solomon, S.C.; Zwally, H.J.; et al. Mars Orbiter Laser Altimeter: Experiment summary after the first year of global mapping of Mars. *J. Geophys. Res. Planets* **2001**, *106*, 23689–23722. [CrossRef]
22. Morgan, G.A.; Putzig, N.E.; Perry, M.R.; Sizemore, H.G.; Bramson, A.M.; Petersen, E.I.; Bain, Z.M.; Baker, D.M.H.; Mastrogiuseppe, M.; Hoover, R.H.; et al. Availability of subsurface water-ice resources in the northern mid-latitudes of Mars. *Nat. Astron.* **2021**, *5*, 230–236. [CrossRef]
23. Putzig, N.E.; Phillips, R.J.; Campbell, B.A.; Mellon, M.T.; Holt, J.W.; Brothers, T.C. SHARAD soundings and surface roughness at past, present, and proposed landing sites on Mars: Reflections at Phoenix may be attributable to deep ground ice. *J. Geophys. Res. Planets* **2014**, *119*, 1936–1949. [CrossRef]
24. Plaut, J.J.; Picardi, G.; Safaeinili, A.; Ivanov, A.B.; Milkovich, S.M.; Cicchetti, A.; Kofman, W.; Mouginot, J.; Farrell, W.M.; Phillips, R.J.; et al. Subsurface Radar Sounding of the South Polar Layered Deposits of Mars. *Science* **2007**, *316*, 92–95. [CrossRef]
25. Heggy, E.; Clifford, S.M.; Cosmidis, J.; Humeaux, A.; Boisson, J.; Morris, R.V. Geoelectrical Model of the Martian North Polar Layered Deposits. In Proceedings of the 39th Annual Lunar and Planetary Science Conference, League City, TX, USA, 10–14 March 2008; Volume 39, p. 2471.
26. Shoemaker, E.S.; Carter, L.M.; Garry, W.B.; Morgan, G.A.; Plaut, J.J. New Insights Into Subsurface Stratigraphy Northwest of Ascraeus Mons, Mars, Using the SHARAD and MARSIS Radar Sounders. *J. Geophys. Res. Planets* **2022**, *127*, e2022JE007210. [CrossRef]
27. Campbell, B.A.; Morgan, G.A. Fine-Scale Layering of Mars Polar Deposits and Signatures of Ice Content in Nonpolar Material From Multiband SHARAD Data Processing. *Geophys. Res. Lett.* **2018**, *45*, 1759–1766. [CrossRef]
28. Heggy, E.; Paillou, P.; Ruffie, G.; Malezieux, J.M.; Costard, F.; Grandjean, G. On water detection in the martian subsurface using sounding radar. *Icarus* **2001**, *154*, 244–257. [CrossRef]
29. Heggy, E.; Clifford, S.M.; Grimm, R.E.; Dinwiddie, C.L.; Wyrick, D.Y.; Hill, B.E. Ground-penetrating radar sounding in mafic lava flows: Assessing attenuation and scattering losses in Mars-analog volcanic terrains. *J. Geophys. Res. Planets* **2006**, *111*. [CrossRef]
30. Boivin, A.L.; Tsai, C.-A.; Hickson, D.C.; Ghent, R.R.; Daly, M.G. Determination of Broadband Complex EM Parameters of Powdered Materials: 2. Ilmenite-Bearing Lunar Analogue Materials. *J. Geophys. Res. Planets* **2022**, *127*, e2022JE007200. [CrossRef]
31. Campbell, B.; Carter, L.; Phillips, R.; Plaut, J.; Putzig, N.; Safaeinili, A.; Seu, R.; Biccari, D.; Egan, A.; Orosei, R. SHARAD radar sounding of the Vastitas Borealis Formation in Amazonis Planitia. *J. Geophys. Res. Planets* **2008**, *113*, E12010. [CrossRef]
32. Richter, P.H. Estimating Errors in Least-Squares Fitting. *Telecommun. Data Acquis. Prog. Rep.* **1995**, *122*, 107–137.
33. Grima, C.; Kofman, W.; Mouginot, J.; Phillips, R.J.; Hérique, A.; Biccari, D.; Seu, R.; Cutigni, M. North polar deposits of Mars: Extreme purity of the water ice. *Geophys. Res. Lett.* **2009**, *36*, L03203. [CrossRef]
34. Castaldo, L.; Mège, D.; Gurgurewicz, J.; Orosei, R.; Alberti, G. Global permittivity mapping of the Martian surface from SHARAD. *Earth Planet. Sci. Lett.* **2017**, *462*, 55–65. [CrossRef]
35. Petersen, E.I.; Holt, J.W.; Levy, J.S. High Ice Purity of Martian Lobate Debris Aprons at the Regional Scale: Evidence From an Orbital Radar Sounding Survey in Deuteronilus and Protonilus Mensae. *Geophys. Res. Lett.* **2018**, *45*, 11595–11604. [CrossRef]
36. Lalich, D.E.; Holt, J.W.; Smith, I.B. Radar Reflectivity as a Proxy for the Dust Content of Individual Layers in the Martian North Polar Layered Deposits. *J. Geophys. Res. Planets* **2019**, *124*, 1690–1703. [CrossRef]
37. Christensen, P.R.; Jakosky, B.M.; Kieffer, H.H.; Malin, M.C.; McSween, H.Y.; Nealson, K.; Mehall, G.L.; Silverman, S.H.; Ferry, S.; Caplinger, M.; et al. The Thermal Emission Imaging System (THEMIS) for the Mars 2001 Odyssey Mission. *Space Sci. Rev.* **2004**, *110*, 85–130. [CrossRef]
38. Edwards, C.S.; Nowicki, K.J.; Christensen, P.R.; Hill, J.; Gorelick, N.; Murray, K. Mosaicking of global planetary image datasets: 1. Techniques and data processing for Thermal Emission Imaging System (THEMIS) multi-spectral data. *J. Geophys. Res. Planets* **2011**, *116*. [CrossRef]
39. Tanaka, K.L.; Skinner, J.A.; Dohm, J.M.; Irwin, R.P., III; Kolb, E.J.; Fortezzo, C.M.; Platz, T.; Michael, G.G.; Hare, T.M. *Geologic map of Mars*; Scientific Investigations Map; US Geological Survey: Reston, VA, USA, 2014; p. 48.
40. Meng, X.; Xu, Y.; Xiao, L.; Xiao, Z. Permittivity Estimation of Subsurface Deposits in the Elysium–Utopia Region on Mars with MRO Shallow Radar Sounder Data. *Astron. J.* **2020**, *159*, 156. [CrossRef]

41. Ganesh, I.; Carter, L.M.; Smith, I.B. SHARAD mapping of Arsia Mons caldera. *J. Volcanol. Geotherm. Res.* **2020**, *390*, 106748. [CrossRef]
42. Russell, P.S.; Head, J.W. Elysium-Utopia flows as mega-lahars: A model of dike intrusion, cryosphere cracking, and water-sediment release. *J. Geophys. Res. Planets* **2003**, *108*. [CrossRef]
43. Petersen, E.I.; Holt, J.W. Surface Roughness Prevents Radar Penetration of Some Martian Debris-Covered Glaciers. *IEEE Trans. Geosci. Remote Sens.* **2022**, *60*, 5104307. [CrossRef]
44. Morgan, G.A.; Campbell, B.A.; Carter, L.M.; Plaut, J.J. Evidence for the episodic erosion of the Medusae Fossae Formation preserved within the youngest volcanic province on Mars. *Geophys. Res. Lett.* **2015**, *42*, 7336–7342. [CrossRef]
45. Stillman, D.E.; Grimm, R.E. Radar penetrates only the youngest geological units on Mars. *J. Geophys. Res. Planets* **2011**, *116*. [CrossRef]
46. Mellon, M.T.; Jakosky, B.M.; Postawko, S.E. The persistence of equatorial ground ice on Mars. *J. Geophys. Res. Planets* **1997**, *102*, 19357–19369. [CrossRef]
47. Heggy, E.; Clifford, S.M.; Younsi, A.; Miane, J.L.; Carley, R.; Morris, R.V. On the Dielectric Properties of Dust and Ice-Dust Mixtures: Experimental Characterization of the Martian Polar-layered Deposits Analog Materials. In Proceedings of the 38th Annual Lunar and Planetary Science Conference, League City, TX, USA, 12–16 March 2007; Volume 38, p. 1756.
48. Dundas, C.M.; Byrne, S.; McEwen, A.S.; Mellon, M.T.; Wu, M.R.; Daubar, I.; Saper, L. Observations of Ice-Exposing Impacts on Mars over Three Mars Years. *AGU Fall Meet. Abstr.* **2013**, *1*, P31C-07.
49. Piqueux, S.; Buz, J.; Edwards, C.S.; Bandfield, J.L.; Kleinböhl, A.; Kass, D.M.; Hayne, P.O.; Mcs, T.; Teams, T. Widespread Shallow Water Ice on Mars at High Latitudes and Mid Latitudes. *Geophys. Res. Lett.* **2019**, *46*, 14290–14298. [CrossRef]
50. Campbell, B.A.; Watters, T.R.; Morgan, G.A. Dielectric Properties of the Medusae Fossae Formation and Implications for Ice Content. *J. Geophys. Res. Planets* **2021**, *126*, e2020JE006601. [CrossRef]
51. Kerber, L.; Head, J.W.; Madeleine, J.-B.; Forget, F.; Wilson, L. The dispersal of pyroclasts from Apollinaris Patera, Mars: Implications for the origin of the Medusae Fossae Formation. *Icarus* **2011**, *216*, 212–220. [CrossRef]
52. Kreslavsky, M.A.; Head, J.W. Mars: Nature and evolution of young latitude-dependent water-ice-rich mantle. *Geophys. Res. Lett.* **2002**, *29*, 14-1–14-4. [CrossRef]